PHYSICS

Hydrodynamic synchronization and clustering in ratcheting colloidal matter

Sergi G. Leyva[1,2]†, Ralph L. Stoop[1]†, Ignacio Pagonabarraga[1,2,3], Pietro Tierno[1,2,4]*

Ratchet transport systems are widespread in physics and biology; however, the effect of the dispersing medium in the collective dynamics of these out-of-equilibrium systems has been often overlooked. We show that, in a traveling wave magnetic ratchet, long-range hydrodynamic interactions (HIs) produce a series of remarkable phenomena on the transport and assembly of interacting Brownian particles. We demonstrate that HIs induce the resynchronization with the traveling wave that emerges as a "speed-up" effect, characterized by a net raise of the translational speed, which doubles that of single particles. When competing with dipolar forces and the underlying substrate symmetry, HIs promote the formation of clusters that grow perpendicular to the driving direction. We support our findings both with Langevin dynamics and with a theoretical model that accounts for the fluid-mediated interactions. Our work illustrates the role of the dispersing medium on the dynamics of driven colloidal matter and unveils the growing process and cluster morphologies above a periodic substrate.

INTRODUCTION

The directional transport of microscopic entities in fluid media occurs in several physical and biological processes ranging from the nanoparticle delivery in a microfluidic network (1, 2) to liquid sliding across topographic surfaces (3, 4), translocation of proteins (5), molecular motors (6, 7), or enzymes (8). At the microscale, thermal fluctuations can be converted into directed motion via the ratchet effect, which uses spatial or temporal asymmetries in the system to generate a preferred direction of motion (9, 10). Technological progresses in engineering external potentials have shown that colloidal particles represent an experimentally accessible model system to investigate ratchet transport effects (11–16). Beyond the colloidal domain, realizing particle-based ratchets may also be of interest for other research fields, since a similar transport scheme can be extended to other systems on different length scales (17–20). However, many experimental realizations have focused on proposing scheme for single particles, or few interacting ones, neglecting the effect of the dispersing medium. Such effect may become important in many-body systems, affecting the particle transport and also leading to unexpected emergent phenomena.

The dynamics of microscopic particles in liquid media often occurs at low Reynolds number (Re), where inertial forces are negligible and fluid mechanic laws become time reversible. Under such conditions, hydrodynamic interactions (HIs), namely, fluid-mediated long-range interactions, may become important since they are excited by the diffusive or driven motion of the dispersed particles. These interactions have been invoked as essential in many physical and biological systems and lead to several fascinating phenomena from the spontaneous formation of vortex colonies (21) or the circular path of the bacteria Escherichia coli (21), to the synchronized beating of cilia (22). Apart from biological systems, there are several

examples where HIs play a crucial role in the organization (23–25) and dynamics (26–28) of micrometer-scale particles. When considering particles driven via a ratchet effect, the role of HIs has been often overlooked, giving more emphasis on other types of interactions such as steric (29), optic (30), electrostatic (31), or geometric (32) ones. Thus, understanding the role of HIs often hidden in such systems, although challenging, will shed light on novel physical effects that could occur in other soft or biological systems on similar length scales.

Here, we investigate the collective dynamics and the effect of HIs in a ratcheting colloidal system based on a magnetic traveling wave. We show that, by raising the particle density, these interactions modify the particle dynamics, leading to a series of emerging phenomena. These include a "speed-up" effect characterized by a substantial raise of the particle speed due to the resynchronization with the translating potential and a synchronized clustering during transport. In the latter case, we find a novel mechanism for cluster growth and morphology originated by the underlying symmetry of the substrate.

To elucidate the fundamental physical mechanisms in our system, we complement the experimental results with theory and numerical simulations.

RESULTS

The magnetic ratchet

Our driven colloidal system is based on a ferrite garnet film (FGF), which displays at zero applied field a pattern of parallel ferromagnetic domains with alternating up and down magnetization, and a spatial periodicity of $\lambda = 2.6$ μm (Fig. 1A). On the surface of the FGF, the stray field generates a sinusoidal-like magnetic potential composed of a series of equispaced minima located at a distance λ. Above this platform, we deposit paramagnetic polystyrene microspheres with diameter $d = 2.8$ μm and magnetic volume susceptibility $\chi \sim 0.4$ (Dynabeads M-270, Invitrogen). These particles are doped with nanoscale iron oxide grains, and they feature a paramagnetic behaviour acquiring an induced moment $\boldsymbol{m} = V\chi\boldsymbol{H}_{tot}$ under an external field $\boldsymbol{H}_{tot}$, where $V = (\pi d^3)/6$. Once above the film, the particles form a two-dimensional (2D) monolayer with negligible out-of-plane motion due to the magnetic attraction toward the Bloch
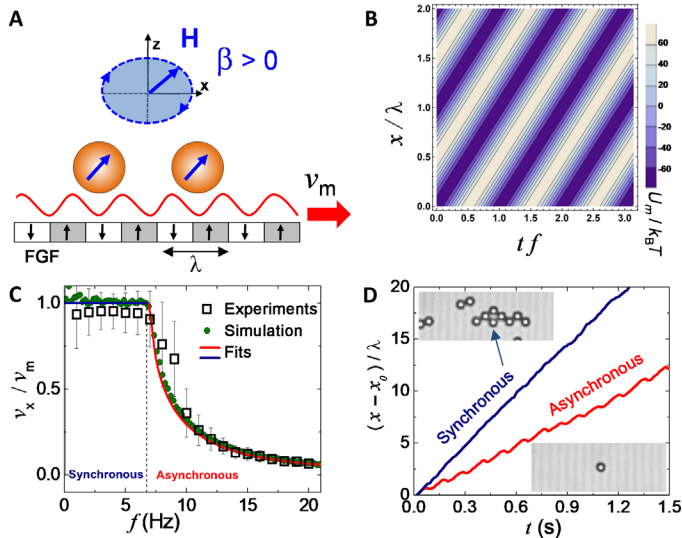
Fig. 1. The magnetic ratchet system. (**A**) Schematic of the magnetic traveling wave: A sinusoidal potential (wavelength $\lambda = 2.6\,\mu m$) is generated above the surface of an FGF. The potential translates at a speed $v_m = \lambda f$ under the action of an elliptically polarized rotating field H with frequency f and ellipticity β. (**B**) Calculated energy landscape of one driven particle showing the time evolution of low (high) energy corridors in blue (white). (**C**) Normalized single-particle speed v_x versus frequency f from experiments (open symbols) and numerical simulation (filled symbols). Continuous lines are fit to the synchronous (blue) and sliding (red) regimes. (**D**) Normalized position $(x - x_0)/\lambda$ versus time t of a single particle (red line, bottom image) and a particle in a rhombic cluster (blue line, top image). In both cases, $f = 8$ Hz and $\beta = -0.4$, which corresponds to asynchronous regime for the individual particle, and x_0 is the position at time $t = 0$ s. The movement of pair of particles in the asynchronous regime is shown in movie S1.

walls. Further details on the preparation of the FGF film are given in Materials and Methods.

We manipulate and transport the particles above the FGF by applying an external rotating field elliptically polarized in the (x, z) plane with frequency f

$$\boldsymbol{H}(t) \equiv [H_x \cos(2\pi f t)\, \boldsymbol{e}_x - H_z \sin(2\pi f t)\, \boldsymbol{e}_z] \quad (1)$$

Here, H_x, H_z are the amplitudes along the x, z axis, where $H_0 = \sqrt{(H_x^2 + H_z^2)/2}$ is the total amplitude. The elliptical polarization of the applied field is controlled by the parameter $\beta = (H_x^2 - H_z^2)/(H_x^2 + H_z^2)$, which will be used to tune the dipolar interactions. Here, $\beta > 0$ ($\beta < 0$) corresponds to $H_x > H_z$ ($H_x < H_z$), i.e., a higher in-plane (out-of-plane) field component. This time-dependent field modulates the stray magnetic field on the FGF surface and leads to a translating spatially periodic magnetic energy landscape,

$$U_m = -U_0 \cos\left[\frac{2\pi}{\lambda}(x - v_m t)\right]$$ as shown in Fig. 1B. Here, U_0 is the

potential amplitude (see later) and $v_m = \lambda f$ is the speed of the traveling wave. As a consequence of this modulation, the magnetic landscape transports colloidal particles that are trapped in its energy minima.

Figure 1C illustrates the main feature of the single-particle transport and combines experiments and simulation data (see later), demonstrating the quantitative agreement between both. By raising the driving frequency, we find two dynamic regimes, separated by a

critical frequency $f_c = 6.7$ Hz. The first regime is a phase-locked motion ($f < f_c$) where the particle moves with the speed of the traveling wave, $v_x = v_m$. For $f > f_c$, the particle desynchronizes with the traveling wave (sliding regime), and its average speed decreases as

$$v_x = v_m(1 - \sqrt{1 - f_c^2/f^2}) < v_m \text{ (Fig. 1C). In the latter regime, the}$$

traveling wave becomes too fast and the loss of synchronization results from the viscous drag that overcomes the magnetic driving. As we are interested in the collective resynchronization effect due to HIs, we drive our particles above f_c, fix for all experiments the total amplitude $H_0 = 850$ A m^{-1}, and vary mainly β and the normalized surface density $\tilde{\rho} = N\pi(d/2)^2/A$, where N is the number of particles located in area A. An illustrative example of the difference between synchronous and asynchronous regimes is shown in Fig. 1D (see also movie S1), which shows the evolution of the position along the driving direction for a single particle and a particle in a rhombic-like cluster. In both cases, the driving frequency is $f = 8$ Hz ($\beta = -0.4$) so that the position of the individual particle (image at the bottom) displays a series of characteristic oscillations due to the loss of synchronization with the traveling wave. These small delay leads to a reduction of the mean speed and thus of the slope. As we will discuss in the next section, we find that a particle in a cluster displays a speed-up effect for frequencies $f > f_c$ that enhances synchronization with the traveling wave, reaching a maximum speed equal to v_m.

Particle interaction and speed-up

Above the FGF, the paramagnetic colloids interact mainly via dipolar forces and HIs. The first types of interactions (we come back to HIs later) can be tuned by varying the parameter β (*33*). For two particles above the FGF plane, the threshold ellipticity that separates the dipolar interactions from attractive to repulsive is given by $\beta_c = -1 + 2/(3\cos_2\vartheta)$, where ϑ is the polar angle that connects the x axis with the distance r between the particle centers. As shown in Fig. 2A, when particles are aligned along the x axis ($\vartheta = 0$), magnetic attraction (repulsion) arises for $\beta > -1/3$ ($\beta < -1/3$), and close to $\beta_c = -1/3$, such interactions are minimized. This dependence of dipolar interactions on β allows to manifest the effect of HIs in both attractive and repulsive scenarios.

Figure 2B shows the results of a series of experiments where we systematically vary the surface density $\tilde{\rho}$ and measure the collective particle speed along the driving direction (x), $\bar{v}_x$, for different values of β, all in the asynchronous regime ($f = 8$ Hz $> f_c$). We find that for $\tilde{\rho} > 0.2$, the colloidal particles resynchronize with the traveling wave reaching the maximum speed of $v_m = 20.8\,\mu m\,s^{-1}$, much higher than that of a single particle, for example, $v_x = 7\,\mu m\,s^{-1}$ for all $\beta > 0$. This remarkable speed-up effect is rather robust, spanning a wide range of densities $\tilde{\rho} \in [0.2, 0.65]$. Further, this speed-up is observed for both attractive and repulsive dipolar interactions $\beta \in [-0.6, 0.6]$, which leads us to exclude magnetic dipolar interactions as the main reason for the observed resynchronization. Collective velocities of the order $\bar{v}_x \in [6, 20.8]\,\mu m\,s^{-1}$ correspond to relatively large Péclet numbers $Pe \in [84, 291]$; thus, the generated hydrodynamic flow becomes progressively more important and must inevitably affect the particle motion. Here, we calculate the Péclet number Pe as the ratio between the Brownian time τ_B required by the particle to diffuse its own radius and the driven time τ_D required to move its radius due to the magnetic landscape. Here, $\tau_D = d^2/(4D_{eff})$, where $D_{eff} = 0.14\,\mu m^2\,s^{-1}$ is the effective diffusion coefficient of the paramagnetic colloid, and $\tau_D = d/(2v_x)$. We further note that for $\beta > 0.2$, the collective speed
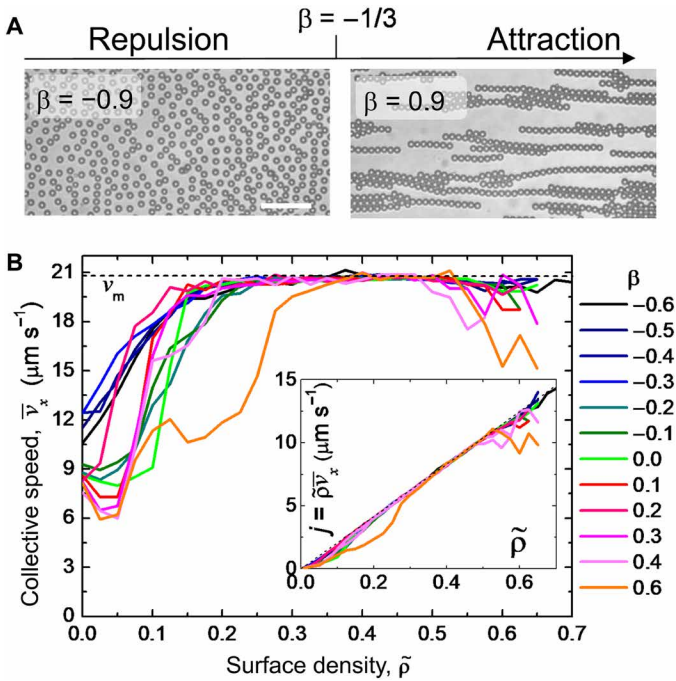
Fig. 2. Experimental current density diagram. (A) Experimental images showing translating repulsive particles (β = −0.9 < 1/3) and chains (β = 0.9 > 1/3) in the sliding regime with $f = 8$ Hz. Scale bar, 20 μm (left). See also corresponding movies S2 and S3. (B) Collective particle speed $\bar{v}_x$ versus normalized surface density $\tilde{\rho}$ for different values of β. Dashed line corresponds to $v_m = 20.8\,\mu\text{m s}^{-1}$. Inset shows the corresponding linear raise of the particle flux $j = \tilde{\rho}\bar{v}_x$ versus $\tilde{\rho}$.

decreases at large densities, $\tilde{\rho} > 0.5$ (Fig. 2B). In this situation, the strong dipolar forces induce the formation of elongated and compact trains (Fig. 2A, right), where HIs are weakened because of the reduced space between the particles. In this situation, the chains recover the asynchronous regime and the system displays an overall reduction of the average speed. We note that in our system, we never observe a reverse of the particle current due to the spatial symmetry of the translating periodic potential. However, a current reversal could be realized by either preparing a special magnetic modulation that would produce a spatially asymmetric potential (34) or adding a bias force against the flow that would tilt the potential.

DISCUSSION
Numerical simulation
The emerging dynamics observed in our driven colloidal system result from the combined action of different interactions, including magnetic dipolar and hydrodynamics ones. To understand their relative role in the system, we perform Brownian dynamic simulations (see Fig. 1C). For each particle i at position r_i, we integrate the overdamped equation of motion

$$\gamma\frac{d\boldsymbol{r}_i}{dt} = \boldsymbol{F}_i^{\text{ext}} + \sum_{j\neq i}\boldsymbol{F}_i^{\text{dip}} + \sum_{j\neq i}\boldsymbol{F}_i^{\text{int}} + \gamma\boldsymbol{v}_i^H + \xi \qquad (2)$$

where γ is the friction coefficient, $\boldsymbol{F}_i^{\text{ext}}$ is the external driving force resulting from the traveling wave, $\boldsymbol{F}_i^{\text{dip}}$ is the total force due to magnetic dipolar interactions, $\boldsymbol{F}_i^{\text{int}}$ accounts for the steric force with the rest of the particles, and ξ is a Gaussian white noise. These forces

reproduce the isolated particle experimental speed, as shown in Fig. 1C. More details on $\boldsymbol{F}_i^{\text{ext}}$, $\boldsymbol{F}_i^{\text{dip}}$, and $\boldsymbol{F}_i^{\text{int}}$ and the parameters used are given in Materials and Methods. To model HIs, we assume that the particles are embedded in a solvent and dragged by the fluid flow of velocity $\boldsymbol{v}_i^H$, generated by the net force acting on the rest of the suspended particles, $\boldsymbol{F}_i(\boldsymbol{r}_i) = \boldsymbol{F}_i^{\text{ext}}(\boldsymbol{r}_i) + \sum_{j\neq i}[\boldsymbol{F}_{ij}^{\text{dip}}(\boldsymbol{r}_{ij}) + \boldsymbol{F}_{ij}^{\text{int}}(\boldsymbol{r}_{ij})]$. We account for this effect with

$$\boldsymbol{v}_i^H = \sum_{j\neq i}^N \boldsymbol{G}_{ij}(\boldsymbol{r}_i,\boldsymbol{r}_j)\boldsymbol{F}_j(\boldsymbol{r}_j) \qquad (3)$$

where $\boldsymbol{G}_{ij}(\boldsymbol{r}_i,\boldsymbol{r}_j)$ stands for the Blake-Oseen mobility tensor (35), which considers the effect of the close proximity of the substrate in the far-field approximation. Last, ξ represents a random force due to thermal fluctuation, with zero mean, $\langle\xi\rangle = 0$, and delta correlated, $\langle\xi(t)\xi(t')\rangle = 2k_BT\gamma\delta(t - t')$.

By integrating Eq. 2, we find that the quantitative agreement with the experimental data can be obtained only by including HIs, even in the absence of dipolar forces. As a representative case, we show in Fig. 3A the collective speed $\bar{v}_x$ for β = − 0.3, where dipolar interactions are slightly repulsive. If we disregard the induced flow, $\boldsymbol{v}_i^H \simeq 0$, and account only for steric and/or magnetic dipolar interactions, the average colloidal speed decreases with the particle density, $\tilde{\rho}$, in contrast to the experimental observations. We note that at large densities, we identify numerically the transition to the asynchronous regime when $\bar{v}_x \sim 0.95\,v_m$. When magnetic interactions are weak (β = − 0.3), increasing $\tilde{\rho}$ raises the speed-up effect and thus f_c due to the hydrodynamic coupling between the particles. The effect is such that at $\tilde{\rho} = 0.6$, the new critical frequency $f_c = 10.3$ Hz almost doubles that of a single particle (see Fig. 3B, bottom line). Increasing the magnetic coupling instead reduces the speed-up effect: For attractive interactions (β > −0.3), the formation of chain weakens HIs, reducing the net particle speed. In the repulsive case (β < − 0.3), particles are forced to span a larger region and this reduces both the hydrodynamic coupling and f_c, as shown in Fig. 3B (top line). We also note that commensurability between the particle size and the wavelength of the underlying pattern in 1D is also important for the synchronization with the moving landscape. By running the simulation along 1D with particles larger than λ, we find that full synchronization was not achieved in opposition to our 2D experimental setup. Thus, a smaller diameter allows the particles to be accommodated in consecutive minima and to be more easily driven by the magnetic landscape.

Theoretical model
To explain the observed synchronization effect, we consider a pair of aligned colloids displacing perpendicular to the FGF and take into account the interplay between the external potential and the HIs. We assume negligible thermal noise and start from the overdamped equation of motion of one particle i

$$\gamma\dot{x}_i = F^e(x,t) + \gamma v_i^H \qquad (4)$$

where the force due to the magnetic potential on such particle at position x_i is

$$F^e(x_i,t) = -16\frac{U_0}{\lambda}\frac{H}{M_s}e^{-2\pi z_0/\lambda}\sin\left[2\pi\left(\frac{x_i}{\lambda} - ft\right)\right] \qquad (5)$$

Here, z_0 is the particle elevation fixed by the balance between gravity and steric repulsion from the solid substrate, $U_0 = \pi d^3\chi\mu_0 M_s^2/6$ is the characteristic magnetic energy, μ_0 is the vacuum permeability,
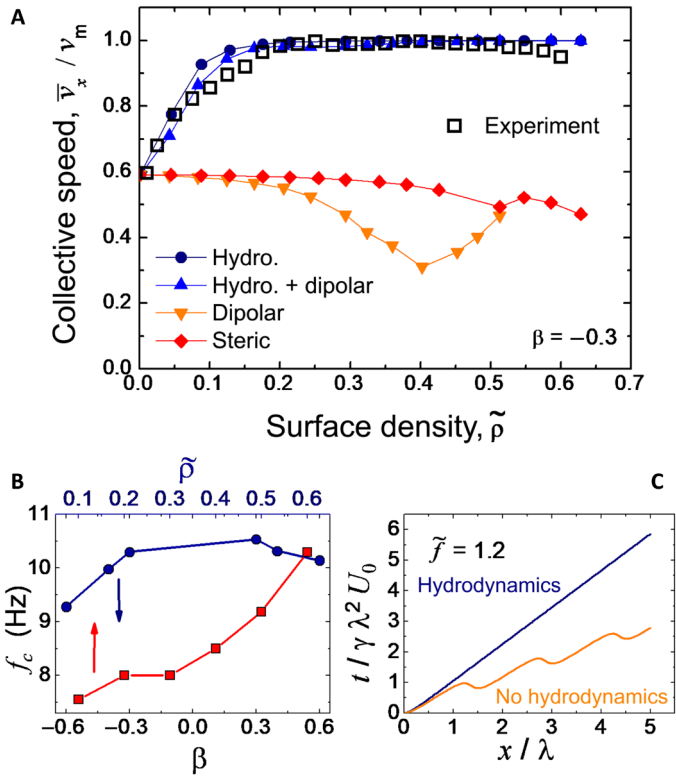
A

B **C**

Fig. 3. Experiment and simulation results. (**A**) Normalized collective speed $\bar{v}_x$ versus surface density $\tilde{\rho}$ from experiments, empty squares ($\beta = -0.3$ and $f = 8$ Hz > f_c), and numerical simulation (Eq. 2) with HIs (filled circles), hydrodynamic and dipolar interactions (upper triangles), only dipolar interactions (lower triangles), and only steric interactions (diamonds). (**B**) Simulations: Critical frequency f_c versus surface density $\tilde{\rho}$ (squares) field ellipticity β (circles) for $\beta = -0.3$ ($\tilde{\rho} = 0.6$). (**C**) Numerical integration of Eq. 9 with and without hydrodynamics for $\tilde{f} = 1.2$.

and $M_s = 1.3 \cdot 10^4$ A m^{-1} is the saturation magnetization of the FGF film (*36*). We rewrite the equation of motion by rescaling length and time with λ and $\gamma\lambda^2/U_0$, respectively, and moving to the reference frame of the traveling wave via the change of variables $q(t) = -x(t)/\lambda + ft$

$$\dot{q}_i(t) = \tilde{f} - \tilde{f}_c\left[\sin\left[2\pi q_i\right] + \frac{3d}{8\lambda}\sum_{j\neq i}^N \bar{G}\left(q_i, q_j\right)\sin\left[2\pi q_j\right]\right] \quad (6)$$

where $\bar{G}(q_i, q_j) = 8\pi\eta\lambda\boldsymbol{e}_x \cdot \boldsymbol{G}(q_i, q_j) \cdot \boldsymbol{e}_x$, and we have introduced the dimensionless parameters $\tilde{f}_c \equiv 16 H_0 e^{-2\pi z_0}/M_s$ and $\tilde{f} \equiv f\gamma\lambda^2/U_0$, where $\gamma = 3\pi\eta d$ is the viscous friction in a medium of viscosity η. We note that the essence of the role played by the hydrodynamic coupling is captured already with the Oseen tensor; the substrate contributes quantitatively to the ratio $\tilde{f}_h/\tilde{f}_c$. For the Oseen-Blake tensor

$$\bar{G}(q_i, q_j) = \frac{2}{\Delta_{ij}}\left[1 - \frac{1 + \epsilon_{ij} + \frac{3}{4}\epsilon_{ij}^2}{(1 + \epsilon_{ij})^{5/2}}\right] \quad (7)$$

where $\Delta_{ij} \equiv |q_i - q_j|$ and $\epsilon_{ij} \equiv \left(\frac{2h}{\Delta_{ij}}\right)^2$, while for the Oseen tensor, $\bar{G}(q_i, q_j) = \frac{2}{\Delta_{ij}}$. In Eq. 6, the contribution of the HIs appears from the second term in the right hand side, while in the absence of HIs, we obtain the single-particle behavior characterized in Fig. 1C. In this case, the solution $\dot{q} = 0$ is only possible when $\tilde{f} < \tilde{f}_c$, where the

particle is synchronized with the traveling wave. To analyze the impact of HIs, for simplicity, we assume that the particles are equidistantly distributed above the traveling wave with periodicity λ, which allows factorizing Eq. 6 as

$$\dot{q}_i(t) = \tilde{f} - \tilde{f}_c\sin\left[2\pi q_i\right]\left[1 + \frac{3d}{8\lambda}\sum_{j\neq i}^N \bar{G}(q_i, q_j)\right] \quad (8)$$

Synchronous motion, $\dot{q} = 0$, occurs when $\sin\left[2\pi q_i\right] = \tilde{f}/\tilde{f}_c\left[1 + \frac{3d}{8\lambda}\sum_{j\neq i}^N \bar{G}(q_i, q_j)\right]$, which is allowed for frequencies $\tilde{f} < \tilde{f}_h \equiv \tilde{f}_c\left[1 + \frac{3d}{8\lambda}\sum_{j\neq N/2}^N \bar{G}(q_{N/2}, q_j)\right]$. Since $\bar{G}(q_i, q_j) > 0$, $\tilde{f}_h > \tilde{f}_c$, HIs increase the frequency range where the synchrony with the traveling wave is sustained. In particular, HIs displace the critical frequency of an amount $\delta\tilde{f} = \tilde{f}_h - \tilde{f}_c$, which increases with the number N of colloidal particles. The confinement due the solid substrate decreases $\tilde{f}_h$ monotonously as the colloids approach the wall; at contact, $\delta\tilde{f} = 0$.

We further note that the momentum exchange with the substrate can alter qualitatively the range of frequencies over which the synchronization is sustained. For example, $\tilde{f}_h$ doubles its magnitude when the colloids come into contact with a slip substrate with respect to its magnitude in an unbounded medium. For a slip planar interface, we find that the Oseen-Blake tensor is given by $\bar{G}(q_i, q_j) = \frac{2}{\Delta_{ij}}\left[1 + \frac{1}{(1 + \epsilon_{ij})^{1/2}}\right]$.

Colloidal synchronization and assembly

The hydrodynamic-induced synchronization is due to the net drag generated by the flow of the rest of the colloidal particles as they are propelled by the magnetic traveling wave. The underlying mechanism is already apparent when analyzing the motion of a pair of driven colloids, where Eq. 8 reduces to

$$\dot{q}_i = \tilde{f} - \tilde{f}_c\sin\left[2\pi q_i\right] - \tilde{f}_c\frac{F_h\sin\left[2\pi q_j\right]}{|q_i - q_j|}, i, j = 1, 2(i \neq j) \quad (9)$$

with $F_h = 3d/4\lambda$ the normalized strength of the HIs, and where, for simplicity, we disregard the effect of the substrate. Accordingly, in this case, $\bar{G}(q_i, q_j) = \frac{2}{|q_i - q_j|}$ and a pair of particles a distance Δ away will displace synchronously up to $\tilde{f}_h = \tilde{f}_c(1 + F_h/\Delta)$. Figure 3C shows the trajectories for two colloids initially at a distance equal to $\Delta = \lambda$, for which $\tilde{f}_h/\tilde{f}_c = 3/2$. Above $\tilde{f}_c$, the colloids slip with respect to the underlying moving substrate in the absence of HI, while they move synchronously due to the additional hydrodynamic drag until $\tilde{f}_h$.

Equation 9 not only shows that already a pair of particles produces hydrodynamic synchronization but also suggests a growing mechanism for colloidal clusters. Aggregates formed by synchronized particles travel faster than asynchronous colloids. After a collision, the particles attach to the synchronous cluster and increase their velocity to lock with the traveling wave. We can also apply our model to other driven colloidal systems that display HIs. For example, Lutz *et al.* (*37*) reported that optically trapped colloids subjected to a constant force on a toroidal potential display a speed enhancement due to HIs. As shown in the Supplementary Materials, if we apply our model to such situation, we find that HIs lead to an increase of the particle velocity, but only when the particles surmount the energetic barrier of the optical potential.

HIs also play a determinant role in the emerging colloidal morphologies. When $\beta > -1/3$, attractive dipolar interactions induce

chain formation along the direction of motion, x, due to the effective repulsion that the particles experience when moving transversally. However, we experimentally observe that, up to $\beta \sim 0.7$, the particles self-assemble into traveling clusters with a characteristic rhombic-like ordering spanning both directions; a typical case is shown in Fig. 4A with $\beta = 0.4$.

We characterize the aggregation process in terms of the cluster variance along the driving direction, $\sigma_x = \frac{1}{N_c}\sum_{i=1}^{N_c}(x_{cm} - x_i)^2$, where x_{cm} is the center of mass and N_c is the number of particles in the cluster. Figure 4C displays σ_x, normalized by σ_t, the latter being the variance of a perfect chain, when N_c particles are in close contact moving along a straight line. In the absence of HIs, $\sigma_x/\sigma_t \sim 1$ for most of the cluster length, which corresponds to the situation depicted in Fig. 4D. Similarly, as shown in the inset of Fig. 4B, the cluster anisotropy parameter $\phi = |\sigma_x - \sigma_y|/(\sigma_x + \sigma_y)$ is maximal in absence of HIs, while it vanishes by increasing N_c with HIs. These results highlight that, in the presence of a periodic substrate, HIs and dipolar forces promote the formation of colloidal aggregates, with sizes and symmetries not allowed on a simple plane.

The rhombic-like ordering results from the competition between the size of the colloidal particles and the periodicity of the magnetic landscape, in the presence of dipolar and HIs. Dipolar interactions attract particles and set them in contact at a distance d. HIs synchronize

the particles at a distance λ along the driving direction (x). Thus, particles at close contact have a transverse distance $l_d = \sqrt{d^2 - \lambda^2}$ (see small inset in Fig. 4B). Thus, the contribution of HIs to the cluster morphology consists of a drag force that synchronizes particles, placing them at a characteristic distance λ along the x direction. In the experimental system, we find that the ratio $d/\lambda = 0.92$, which sets a transversal length between particles in the cluster of $l_d \simeq 0.28$. Now, decreasing the ratio d/λ gives a larger transversal length and a larger area covered by the clusters along the transverse direction. In contrast, increasing d/λ to unity leads to the formation of synchronized particles that travel in the form of trains of particles. In such case, even at large $\beta > 0$, the synchronicity with the traveling wave is not lost due to the presence of HIs. We further note that rhombic ordering is reminiscent of the equilibrium structure predicted for 2D colloidal systems, with interactions that compete with the symmetry of an underlying substrate (38). However, the morphologies we observe develop from the interplay between the ratchet potential coupled to HIs and the magnetic dipolar interactions, as unveiled by our numerical simulations in Fig. 4B. The exclusion of HIs by setting $\mathbf{v}_i^H = 0$ leads to the formation of traveling chains, as shown in Fig. 4C.

To conclude, we have investigated the role of HIs on the collective dynamics of microscopic particles driven above a translating magnetic
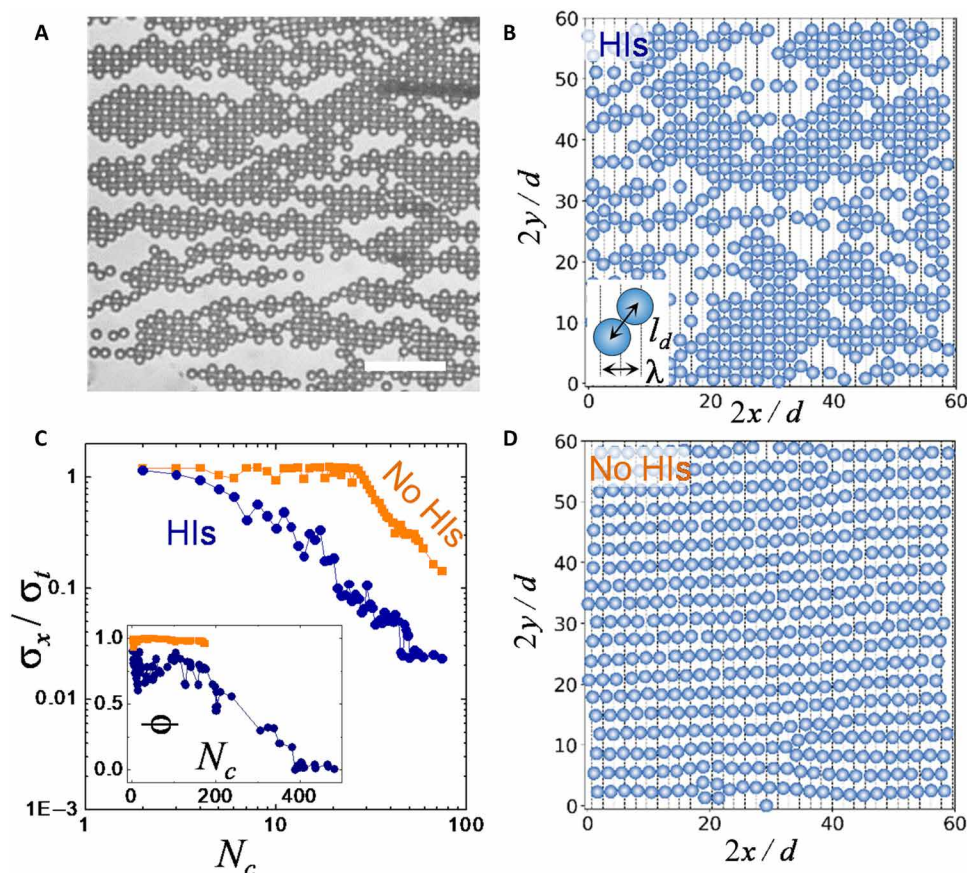

Fig. 4. Collective propulsion and assembly. Experimental (**A**) and simulation (**B** and **D**) snapshots of anisotropic clusters propelled by a rotating field with $\beta = 0.4$. Scale bar, 20 μm (A). Bottom scheme in (B) illustrates the transverse distance l_d. See movie S4. In (B) [(D)], the simulation was run with [without] HIs. (**C**) Simulations: Relative cluster dispersion σ_x/σ_t versus number of particles in the cluster N_c with (blue) and without (orange) HIs. Inset shows the corresponding cluster anisotropy ratio $\phi = |\sigma_x - \sigma_y/(\sigma_x + \sigma_y)|$ versus N_c.

potential. We find that such interactions lead to a substantial raise of the particle speed and favor colloidal arrangements congruent with the periodicity of the underlying substrate. We experimentally observe that such arrangement promotes the emergence of compact rhombic clusters along the potential domains. We rationalize the experimental observations with both theory and numerical simulations. Thus, our system leads to a variability of the morphology of synchronized clusters due to the interplay between the substrate symmetry, hydrodynamic, and dipolar interactions.

Traveling wave ratchets where directed transport is achieved via a sliding periodic potential are present in several soft and condensed matter systems. Examples with microscopic colloids, apart from our garnet film, include electrophoretic (39) or magnetically (40) driven particles above patterned substrates, and in other field include active particles (41), chemotactic fronts (42), defects and asperities in frictional sliding (43), or magnetic flux quanta (44). Thus, with our work, we investigate the role of the dispersing media on the collective particle dynamics and show that it can lead to unexpected phenomena, which could have been overlooked in similar ratchet systems at high density. We also mention that recently, Belovs et al. (45) reported numerically the synchronization of puller type magnetotactic bacteria under a rotating magnetic field. This work confirms the general nature of the phenomena of synchronization due to HIs (46, 47), which we have experimentally observed here with a driven ratchet system.

Ratchet transport schemes have been invoked as simplified models to explain the complex dynamics that occur in many physical and biological systems (48), including micro- and nanomachines (49–52), intracellular transport (53, 54), and even as a way to rectify active matter (55–58). With our colloidal model system, we show the importance of considering HIs and their crucial role in the collective organization of driven microscopic matter.

MATERIALS AND METHODS
Magnetic film and coating
The FGF was grown by dipping liquid-phase epitaxy on a gadolinium gallium garnet substrate; more details can be found in a previous work (59). Before the experiments, we coat the FGF film with a 1-μm-thick layer of a photoresist (AZ-1512 Microchem, Newton, MA) to prevent adhesion of the paramagnetic particles on the substrate. This process was performed via combination of spin coating and backing, following previous work (60). We wash the FGF in highly deionized water (MilliQ, Millipore) before each experiment.

Details of the numerical simulation
In our simulation scheme, we integrate the set of Eq. 2 where the remaining terms on the right hand side, apart from the fourth one (HIs), are described below. The external driving force that is produced by the traveling wave (36) is given by

$$\mathbf{F}^{\text{ext}}(x,t) = F_M\left[u_1(t)\sin\left(\frac{2\pi x}{\lambda}\right) - u_2(t)\cos\left(\frac{2\pi x}{\lambda}\right)\right]\mathbf{e}_x \quad (10)$$

where $u_1(\beta,t) = \sqrt{1+\beta}\cos(2\pi ft)$, $u_2(\beta,t) = \sqrt{1-\beta}\cos(2\pi ft)$, and $F_M = 16H_0 e^{-2\pi z/\lambda}U_0/M_s\lambda$.

$\mathbf{F}_i^{\text{dip}}$ is the dipolar interaction between the paramagnetic particles. For two point dipoles ($\mathbf{m}_i$, $\mathbf{m}_j$) located at position (i, j), it is given by

$$\mathbf{F}^{\text{dip}}(\mathbf{r}_{ij}) = \frac{3\mu_0}{4\pi|\,r_{ij}\,|^4}((\hat{\mathbf{e}}_{ij} \times \mathbf{m}_i) \times \mathbf{m}_j + (\hat{\mathbf{e}}_{ij} \times \mathbf{m}_j) \times \mathbf{m}_i)$$
$$-2\hat{\mathbf{e}}_{ij}(\mathbf{m}_i \cdot \mathbf{m}_j) + 5\hat{\mathbf{e}}_{ij}((\hat{\mathbf{e}}_{ij} \times \mathbf{m}_i) \cdot (\hat{\mathbf{e}}_{ij} \times \mathbf{m}_j))) \quad (11)$$

where $\hat{\mathbf{e}}_{ij}$ is the unitary vector between particle i and j, $\mathbf{r}_{ij} = \mathbf{r}_i - \mathbf{r}_j$, and $\mu_0 = 4\pi \cdot 10^{-7}$ H m. Further, we consider induced point dipoles; thus, for a particle i, the magnetic moment is given by $\mathbf{m}_i = V\chi\mathbf{H}^{\text{tot}}(\mathbf{r}_i)$, where the instantaneous total magnetic field is given by the sum of the external magnetic field and the contribution from the FGF film, $\mathbf{H}^{\text{tot}} = \mathbf{H} + \mathbf{H}^{\text{sub}}$, i.e.

$$\mathbf{H}^{\text{tot}} = (H_x\cos(2\pi ft),0,-H_z\sin(2\pi ft))$$
$$+ \frac{4M_s}{\pi}e^{-2\pi z/\lambda}\left(\cos\left(\frac{2\pi xt}{\lambda}\right),0,-\sin\left(\frac{2\pi xt}{\lambda}\right)\right) \quad (12)$$

Further, $\mathbf{F}_i^{\text{int}}$ is the interaction force between the particles that we derive from a Yukawa-like potential, which accounts for both a short-range repulsion due to electrostatic interactions and the finite particle size. The force between two particles at positions $\mathbf{r}_i$ and $\mathbf{r}_j$ can be written as

$$\mathbf{F}^{\text{int}}(\mathbf{r}_{ij}) = \frac{U_Y}{\lambda_Y}\sum_{i\neq j}^{N}\left[\frac{\sigma}{r_{ij}}\left(\frac{\sigma}{r_{ij}} + \frac{\sigma}{\lambda_Y}e^{-\frac{r_{ij}}{\lambda_Y}}\right) - B\right]\mathbf{e}_{ij} \quad (13)$$

The parameter U_Y quantifies the strength, and λ_Y the characteristic decay length of the Yukawa potential between the interaction of a pair of particles, and $\sigma = d/2$ denotes the radius of the particles. The parameter B is a constant ensuring that the force is zero at the cutoff interaction radius r_c

$$B = \frac{\sigma}{r_c}e^{-\frac{r_c}{\lambda_Y}}\left(\frac{\sigma}{\lambda_Y} + \frac{\sigma}{r_c}\right) \quad (14)$$

Last, ξ represents a random force due to thermal fluctuation, with zero mean, $\langle\xi\rangle = 0$, and delta correlated, $\langle\xi(t)\xi(t')\rangle = 2k_BT\gamma\delta(t-t')$.

To minimize the number of parameters used in the numerical simulation, we rescale length in terms of the radius of the particles $\sigma = d/2$, time in terms of $\tau_D = \gamma d/(2F_M)$, and the magnetic field components in terms of the amplitude H_0. Thus, Eq. 2 can be divided by the characteristic velocity F_M/γ, and Eq. 11 in this dimensional units reduces to

$$\bar{\mathbf{F}}^{\text{dip}} = \frac{F^d}{|\,\bar{r}_{ij}\,|^4}\mathbf{f}(\bar{\mathbf{r}}_{ij},h^{\text{tot}}(\bar{\mathbf{r}}_i),h^{\text{tot}}(\bar{\mathbf{r}}_j)) \quad (15)$$

where F^d is the dipolar strength $F^d = \frac{3\mu_0}{F_M\mu 4\pi}(V\chi)^2$ and $\mathbf{f}(\bar{\mathbf{r}}_{ij},h^{\text{tot}}(\bar{\mathbf{r}}_i),$ $h^{\text{tot}}(\bar{\mathbf{r}}_j))$ is a function that contains the dependences in Eq. 11 involving only the total magnetic field contributions on each particle and the unit vector between two particles. Further, we use a radius of $r_d \simeq 4.5\sigma$ as dipolar cutoff radius is defined, which corresponds to a distance large enough so that contributions of the dipolar interactions are of the order $|\bar{\mathbf{F}}^{\text{dip}}| \simeq 0.05$. As the dipolar force depends not only on distance but also on the joining direction between two particles, the force is imposed to be 0 at r_d using

$$\bar{\mathbf{F}}^{\text{dip}} = F^d\left(\frac{\mathbf{f}(\hat{\mathbf{r}}_{ij},h_i,h_j)}{|\,\bar{r}_{ij}\,|^4} - \frac{\mathbf{f}(\widehat{\mathbf{r}}_{ij},h_i,h_j)}{|\,r_d\,|^4}\right) \quad (16)$$

Equation 2 can be finally rewritten in reduced units as

$$\frac{d\bar{r}_i}{dt} = \frac{U_Y}{\lambda_Y F_M} \sum_{j\neq i} \bar{\boldsymbol{\psi}}(\bar{r}_{ij}) + \bar{\boldsymbol{F}}^{\text{ext}}(\bar{x}_i, \bar{t}) + \bar{\boldsymbol{F}}^{\text{dip}}(\bar{r}_{ij}, h_i, h_j) +$$
$$\frac{1}{F_M}\frac{3}{4}\sum_{j\neq i}^{N} \bar{\boldsymbol{G}}_{ij}(\bar{\boldsymbol{r}}_i, \bar{\boldsymbol{r}}_j)\,\bar{\boldsymbol{F}}(\bar{r}_j) + \sqrt{\frac{2}{Pe}\frac{\tau_D}{dt}}\bar{\xi} \qquad (17)$$

Here, $\bar{r} = r/\sigma$, $\boldsymbol{G}(\boldsymbol{r}_i, \boldsymbol{r}_j) = \frac{3}{4\gamma}\bar{\boldsymbol{G}}(\bar{\boldsymbol{r}}_i, \bar{\boldsymbol{r}}_j)$, and Pe is the Péclet number. In turn, $\bar{\boldsymbol{\psi}} = \bar{\boldsymbol{\psi}}(\bar{r}_{ij})$ is the dimensionless Yukawa force between particles i and j.

As typical experimental values, we use $\gamma = 2.6 \times 10^{-8}$ m N^{-1} s^{-1} and $F_M = 0.1$ pN. The simulation parameters are estimated to be $h_{\text{sub}} = 15.3$, $F^d = 56.1$, Yukawa force strength $U_0/\lambda F_M = 300$, $Pe = 150$, and $\lambda_Y = 1$. Further, comparing the simulations for a single particle and the experiments (Fig. 1C) as a function of the frequency, we can estimate the characteristic time as $\tau_D = 0.075$ s.

SUPPLEMENTARY MATERIALS

REFERENCES AND NOTES
1. S. Matthias, F. Müller, Asymmetric pores in a silicon membrane acting as massively parallel Brownian ratchets. *Nature* **424**, 53–57 (2003).
2. M. J. Skaug, C. Schwemmer, S. Fringes, C. D. Rawlings, A. W. Knoll, Nanofluidic rocking Brownian motors. *Science* **359**, 1505–1508 (2018).
3. I. U. Vakarelski, N. A. Patankar, J. O. Marston, D. Y. C. Chan, S. T. Thoroddsen, Stabilization of Leidenfrost vapour layer by textured superhydrophobic surfaces. *Nature* **489**, 274–277 (2012).
4. S. Feng, P. Zhu, H. Zheng, H. Zhan, C. Chen, J. Li, L. Wang, X. Yao, Y. Liu, Z. Wang, Three-dimensional capillary ratchet-induced liquid directional steering. *Science* **373**, 1344–1348 (2021).
5. H. Mazal, M. Iljina, I. Riven, G. Haran, Ultrafast pore-loop dynamics in a AAA+ machine point to a Brownian-ratchet mechanism for protein translocation. *Sci. Adv.* **7**, eabg4674 (2021).
6. R. D. Astumian, Thermodynamics and kinetics of a Brownian motor. *Science* **276**, 917–922 (1997).
7. D. Keller, C. Bustamante, The mechanochemistry of molecular motors. *Biophys. J.* **78**, 541–556 (2000).
8. J. W. McCausland, X. Yang, G. R. Squyres, Z. Lyu, K. E. Bruce, M. M. Lamanna, B. Söderström, E. C. Garner, M. E. Winkler, J. Xiao, J. Liu, Treadmilling FtsZ polymers drive the directional movement of sPG-synthesis enzymes via a Brownian ratchet mechanism. *Nat. Commun.* **12**, 609 (2021).
9. P. Reimann, Brownian motors: Noisy transport far from equilibrium. *Phys. Rep.* **361**, 57–265 (2002).
10. P. Hänggi, F. Marchesoni, Artificial Brownian motors: Controlling transport on the nanoscale. *Rev. Mod. Phys.* **81**, 387–442 (2009).
11. J. Rousselet, L. Salome, A. Ajdari, J. Prost, Directional motion of Brownian particles induced by a periodic asymmetric potential. *Nature* **370**, 446–447 (1994).
12. L. P. Faucheux, L. S. Bourdieu, P. D. Kaplan, A. J. Libchaber, Optical thermal ratchet. *Phys. Rev. Lett.* **74**, 1504–1507 (1995).
13. K. Gunnarsson, P. E. Roy, S. Felton, J. Pihl, P. Svedlindh, S. Berner, H. Lidbaum, S. Oscarsson, Programmable motion and separation of single magnetic particles on patterned magnetic surfaces. *Adv. Mater.* **17**, 1730–1734 (2005).
14. B. Yellen, O. Hovorka, G. Friedman, Arranging matter by magnetic nanoparticle assemblers. *Proc. Natl. Acad. Sci. U.S.A.* **102**, 8860–8864 (2005).
15. A. Ros, R. Eichhorn, J. Regtmeier, T. T. Duong, P. Reimann, D. Anselmetti, Absolute negative particle mobility. *Nature* **436**, 928 (2005).
16. S.-H. Lee, K. Ladavac, M. Polin, D. G. Grier, Observation of flux reversal in a symmetric optical thermal ratchet. *Phys. Rev. Lett.* **94**, 110601 (2005).
17. J. Frank, R. K. Agrawal, A ratchet-like inter-subunit reorganization of the ribosome during translocation. *Nature* **406**, 318–322 (2000).
18. C. C. de Souza Silva, J. V. de Vondel, M. Morelle, V. V. Moshchalkov, Controlled multiple reversals of a ratchet effect. *Nature* **440**, 651–654 (2006).
19. C. J. O. Reichhardt, C. Reichhardt, Ratchet effects in active matter systems. *Annu. Rev. Condens. Matter Phys.* **8**, 51–75 (2017).
20. S. Park, J. Song, J. S. Kim, In silico construction of a flexibility-based DNA Brownian ratchet for directional nanoparticle delivery. *Science* **5**, eaav4943 (2019).
21. I. H. Riedel, K. Kruse, J. Howard, A self-organized vortex array of hydrodynamically entrained sperm cells. *Science* **309**, 300–303 (2005).
22. A. Vilfan, F. Jülicher, Hydrodynamic flow patterns and synchronization of beating cilia. *Phys. Rev. Lett.* **96**, 058102 (2006).
23. M. Baron, J. Bławzdziewicz, E. Wajnryb, Hydrodynamic crystals: Collective dynamics of regular arrays of spherical particles in a parallel-wall channel. *Phys. Rev. Lett.* **100**, 174502 (2008).
24. Y. Goto, H. Tanaka, Purely hydrodynamic ordering of rotating disks at a finite Reynolds number. *Nat. Commun.* **6**, 5994 (2015).
25. K. Yeo, E. Lushi, P. M. Vlahovska, Collective dynamics in a binary mixture of hydrodynamically coupled microrotors. *Phys. Rev. Lett.* **114**, 188301 (2015).
26. T. M. Squires, M. P. Brenner, Like-charge attraction and hydrodynamic interaction. *Phys. Rev. Lett.* **85**, 4976–4979 (2000).
27. J. Santana-Solano, J. L. Arauz-Lara, Hydrodynamic interactions in quasi-two-dimensional colloidal suspensions. *Phys. Rev. Lett.* **87**, 038302 (2001).
28. A. Grimm, H. Stark, Hydrodynamic interactions enhance the performance of Brownian ratchets. *Soft Matter* **7**, 3219–3227 (2011).
29. P. K. Ghosh, V. R. Misko, F. Marchesoni, F. Nori, Self-propelled janus particles in a ratchet: Numerical simulations. *Phys. Rev. Lett.* **110**, 268301 (2013).
30. A. V. Arzola, M. Villasante-Barahona, K. Volke-Sepúlveda, P. Jákl, P. Zemánek, Omnidirectional transport in fully reconfigurable two dimensional optical ratchets. *Phys. Rev. Lett.* **118**, 138002 (2017).
31. C. Marquet, A. Buguin, L. Talini, P. Silberzan, Rectified motion of colloids in asymmetrically structured channels. *Phys. Rev. Lett.* **88**, 168301 (2002).
32. B. H. Wunsch, J. T. Smith, S. M. Gifford, C. Wang, M. Brink, R. L. Bruce, R. H. Austin, G. Stolovitzky, Y. Astier, Nanoscale lateral displacement arrays for the separation of exosomes and colloids down to 20 nm. *Nat. Nanotechnol.* **11**, 936–940 (2016).
33. A. V. Straube, P. Tierno, Tunable interactions between paramagnetic colloidal particles driven in a modulated ratchet potential. *Soft Matter* **10**, 3915–3925 (2014).
34. F. Martinez-Pedrero, H. Massana-Cid, T. Ziegler, T. H. Johansen, A. V. Straube, P. Tierno, Bidirectional particle transport and size selective sorting of Brownian particles in a flashing spatially periodic energy landscape. *Phys. Chem. Chem. Phys.* **18**, 26353–26357 (2016).
35. J. R. Blake, A note on the image system for a stokeslet in a no-slip boundary. *Proc. Camb. Philos. Soc.* **70**, 303–310 (1971).
36. A. V. Straube, P. Tierno, Synchronous vs. asynchronous transport of a paramagnetic particle in a modulated ratchet potential. *Europhys. Lett.* **103**, 28001 (2013).
37. C. Lutz, M. Reichert, H. Stark, C. Bechinger, Surmounting barriers: The benefit of hydrodynamic interactions. *Europhys. Lett.* **74**, 719–725 (2006).
38. T. Neuhaus, M. Marechal, M. Schmiedeberg, H. Löwen, Rhombic preordering on a square substrate. *Phys. Rev. Lett.* **110**, 118301 (2013).
39. H. Kawamoto, K. Seki, N. Kuromiya, Mechanism of travelling-wave transport of particles. *J. Phys. D Appl. Phys.* **39**, 1249–1256 (2006).
40. B. B. Yellen, R. M. Erb, H. S. Son, R. Hewlin, H. Shang, G. U. Lee, Traveling wave magnetophoresis for high resolution chip based separations. *Lab Chip* **7**, 1681–1688 (2007).
41. C. Sándor, A. Libál, C. Reichhardt, C. J. O. Reichhardt, Collective transport for active matter run-and-tumble disk systems on a traveling-wave substrate. *Phys. Rev. E* **95**, 012607 (2017).
42. R. E. Goldstein, Traveling-wave chemotaxis. *Phys. Rev. Lett.* **77**, 775–778 (1996).
43. M. Hirano, K. Shinjo, Atomistic locking and friction. *Phys. Rev. B Condens. Matter* **41**, 11837–11851 (1990).
44. D. Cole, S. Bending, S. Savel'ev, A. Grigorenko, T. Tamegai, F. Nori, Ratchet without spatial asymmetry for controlling the motion of magnetic flux quanta using time-asymmetric drives. *Nat. Mater.* **5**, 305–311 (2006).
45. M. Belovs, R. Livanovics, A. Cebers, Hydrodynamic synchronization of pairs of puller type magnetotactic bacteria in a high frequency rotating magnetic field. *Soft Matter* **15**, 1627–1632 (2019).
46. J. Kotar, M. Leoni, B. Bassetti, M. Lagomarsino, P. Cicuta, Hydrodynamic synchronization of colloidal oscillators. *Proc. Natl. Acad. Sci. U.S.A.* **107**, 7669–7673 (2010).
47. N. Uchida, R. Golestanian, Generic conditions for hydrodynamic synchronization. *Phys. Rev. Lett.* **106**, 058104 (2011).
48. B. Lau, O. Kedem, J. Schwabacher, D. Kwasnieski, E. A. Weiss, An introduction to ratchets in chemistry and biology. *Mater. Horiz.* **4**, 310–318 (2017).
49. R. D. Astumian, M. Bier, Fluctuation driven ratchets: Molecular motors. *Phys. Rev. Lett.* **72**, 1766–1769 (1994).
50. F. Jülicher, A. Ajdari, J. Prost, Modeling molecular motors. *Rev. Mod. Phys.* **69**, 1269–1282 (1997).
51. P. Malgaretti, I. Pagonabarraga, D. Frenkel, Running faster together: Huge speed up of thermal ratchets due to hydrodynamic coupling. *Phys. Rev. Lett.* **109**, 168101 (2012).

52. S. Kassem, T. van Leeuwen, A. S. Lubbe, M. R. Wilson, B. L. Feringa, D. A. Leigh, Artificial molecular motors. *Chem. Soc. Rev.* **46**, 2592–2621 (2017).

53. C. Appert-Rolland, M. Ebbinghaus, L. Santen, Intracellular transport driven by cytoskeletal motors: General mechanisms and defects. *Phys. Rep.* **593**, 1–59 (2015).

54. C. Hepp, B. Maier, Kinetics of DNA uptake during transformation provide evidence for a translocation ratchet mechanism. *Proc. Natl. Acad. Sci. U.S.A.* **113**, 12467–12472 (2016).

55. P. Galajda, J. Keymer, P. Chaikin, R. Austin, A wall of funnels concentrates swimming bacteria. *J. Bacteriol.* **189**, 8704–8707 (2007).

56. M. B. Wan, C. J. Olson Reichhardt, Z. Nussinov, C. Reichhardt, Rectification of swimming bacteria and self-driven particle systems by arrays of asymmetric barriers. *Phys. Rev. Lett.* **101**, 018102 (2008).

57. L. Angelani, R. Di Leonardo, G. Ruocco, Self-starting micromotors in a bacterial bath. *Phys. Rev. Lett.* **102**, 048104 (2009).

58. R. D. Leonardo, L. Angelani, D. Dell'Arciprete, G. Ruocco, V. Iebba, S. Schippa, M. P. Conte, F. Mecarini, F. De Angelis, E. Di Fabrizio, Bacterial ratchet motors. *Proc. Natl. Acad. Sci. U.S.A.* **107**, 9541–9545 (2010).

59. P. Tierno, F. Sagués, T. H. Johansen, T. M. Fischer, Colloidal transport on magnetic garnet films. *Phys. Chem. Chem. Phys.* **11**, 9615–9625 (2009).

60. P. Tierno, Magnetically reconfigurable colloidal patterns arranged from arrays of selfassembled microscopic dimers. *Soft Matter* **8**, 11443 (2012).